

INFORMATION TO USERS

This dissertation copy was prepared from a negative microfilm created and inspected by the school granting the degree. We are using this film without further inspection or change. If there are any questions about the content, please write directly to the school. The quality of this reproduction is heavily dependent upon the quality of the original material.

The following explanation of techniques is provided to help clarify notations which may appear on this reproduction.

1. Manuscripts may not always be complete. When it is not possible to obtain missing pages, a note appears to indicate this.
2. When copyrighted materials are removed from the manuscript, a note appears to indicate this.
3. Oversize materials (maps, drawings and charts are photographed by sectioning the original, beginning at the upper left hand corner and continuing from left to right in equal sections with small overlaps.

UMI[®]

ProQuest Information and Learning
300 North Zeeb Road, Ann Arbor, MI 48106-1346 USA
800-521-0600

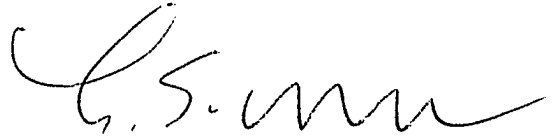
PREVIEW

TORQUE-RELATED LAMELLAR CARBIDE GROWTH ASSOCIATED WITH
ANNEALING TWINS IN 304 STAINLESS STEEL

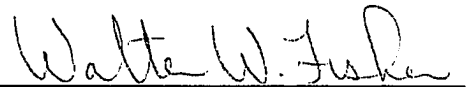
ROBERTA JEAN ROMERO

Metallurgical and Materials Engineering Department

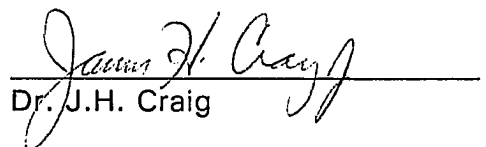
APPROVED:



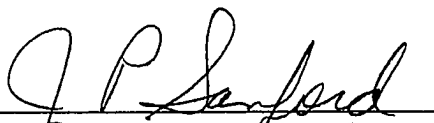
Dr. L.E. Murr, Chairman



Dr. W.W. Fisher



Dr. J.H. Craig



Associate Vice President for
Research and Graduate Studies

PREVIEW

DEDICATION

This thesis is dedicated to two special individuals: first, to the memory of my grandmother, Leonor Murphy Romero, for instilling the motivation and vision to pursue career opportunities which were never offered to her and the women of her generation; and to the memory of my cousin, Jeremiah Carl Gardner, who was full of life and promise but never had the chance to fulfill his dreams in the fifteen years that God had granted him on this earth.

**TORQUE-RELATED LAMELLAR CARBIDE GROWTH ASSOCIATED WITH
ANNEALING TWINS IN 304 STAINLESS STEEL**

by

ROBERTA JEAN ROMERO, B.S. Met. E.

THESIS

Presented to the faculty of the Graduate School of

The University of Texas at El Paso

in Partial Fullfillment

of the Requirements

for the Degree of

MASTER OF SCIENCE

Department of Metallurgical and Materials Engineering

THE UNIVERSITY OF TEXAS AT EL PASO

MAY 1995

ACKNOWLEDGEMENTS

I would like to express my deepest gratitude to Dr. L.E. Murr for his infinite enthusiasm and wisdom. Also, I would like to extend my sincerest appreciation to Dr. A.H. Advani for his guidance, patience, and expertise in electron microscopy with whom I was very fortunate to work with and know. I would like to acknowledge Dr. W.W. Fisher for his expertise in electrochemical issues. In addition, without their contributions, this research would have never been completed, therefore, I would like to extend my deepest gratitude and appreciation to my co-workers Julio Maldonado and Elizabeth Trillo, and Dr. C.S. Niou, for going out of his way to help. I would like to acknowledge Dr. J.H. Craig for his contributions to this thesis. Finally, I would like to thank my family and friends for maintaining my sanity.

This research project was supported by the National Science Foundation (RIMI) HRD 9105065 and the Patricia R. Harris Fellowship.

ABSTRACT

A configurational, equilibrium theory for relative interfacial torques has been invoked to qualitatively explain growth-specific lamellar precipitation of $M_{23}C_6$ carbides in 304 stainless steel where the lamellar growth is always in the $\langle 112 \rangle$ directions coincident with traces of $\{111\}$ planes at 90° to (110) grain surface orientations. For (112) grain surface orientation, $M_{23}C_6$ lamellar growth is always in the $[\bar{1}10]$ direction which is also coincident with traces of $(11\bar{1})$ planes at 90° to the grain surface plane. These $\{111\}$ trace directions for lamellar growth are denoted T90 directions and are shown to coincide with high, relative interfacial torques (or torque configurations) resolved in coherent $\{111\}$ annealing twin boundaries. For grain surface orientations containing annealing twins or twin/grain boundary geometries whose coherent $\{111\}$ boundaries are not consistent with T90 directions, such as (100) , there are no high-torque configurations and no significant lamellar $M_{23}C_6$ growth coincident with $\{111\}$ trace directions.

TABLE OF CONTENTS

Acknowledgements.....	iv
Abstract.....	v
List of Tables.....	viii
List of Figures.....	viii
List of Equations.....	xii

CHAPTER

1.	Introduction.....	1
1.1	Background Narrative.....	1
1.2	Nature of Carbide Precipitation in Stainless Steel.....	5
2.	Experimental Techniques.....	10
2.1	Introduction.....	10
2.2	Materials.....	10
2.3	Sample Preparation.....	11
	2.3.1 Sample Preparation for Mill Processed Stainless Steel.....	12
	2.3.2 Sample Preparation for Thermomechanical Processed Stainless Steel.....	13
	2.3.2.1 Thermomechanical Processing Condition for Grain Size Reduction.....	14
	2.3.2.2 Twin Density Measurement.....	18
2.4	Grain Size Measurements.....	21

2.5	Electrochemical Potentiokinetic Reactivation Test.....	22
2.6	TEM Sample Preparation.....	26
2.7	Electron Microscopy.....	27
3.	Results and Discussion.....	28
3.1	Observations and Theoretical Details.....	28
3.2	Theory of Equilibrium Torques at Twin Boundary-Grain Boundary Intersections.....	37
3.3	Further Tests of Torque Configuration Theory and Predictions for Lamellar Carbide Precipitation.....	50
4.	Conclusions and Recommendations.....	55
4.1	Summary and Conclusions.....	55
4.2	Recommendations for Future Research.....	56
	References.....	58
	Curriculum Vitae.....	61

LIST OF TABLES

- Table 1. Listed are the compositions and respective grain sizes of the four heats of 304 stainless steel.
- Table 2. Listed are strain and aging conditions for 304 stainless steel specimens.
- Table 3. Listed are the conditions and solutions for metallographic examination of grain and twin interfaces of 304 stainless steel.

LIST OF FIGURES

- Fig. 1: Comparison of carbides precipitation at different interfaces in 304 stainless steel (TEM). (a) Grain boundary precipitates. (b) Lamellar growth of carbides precipitates from non-coherent twin boundary. (c) Lamellar carbide growth parallel to $\{111\}$ coherent twin trace. (d) Lamellar carbide growing out from coherent twin plane along another (111) plane. The precipitate appears to be nucleated on a step in the coherent twin boundary.
- Fig. 2: Example of selective EPR-test attack for precipitation and depletion (of Cr) along interfaces in sensitized 304 stainless steel.
- Fig. 3: C-curve for precipitation along specific interfaces in 304 stainless steel having average, specific interfacial free energetics noted. The curves are based on data of Stickler and Vinckier [12]. Grain boundaries denoted (gb), non-coherent twin boundaries are denoted (TB), and coherent twin boundaries are denoted (tb). The corresponding energies are in units of mJ/m_2 [11].
- Fig. 4: Comparison of deformed/annealed microstructures which were etched using 60% nitric solution illustrate significant grain growth occurring at heat treatment times above 1 minute and little or no grain growth below. Specimens were cold rolled to 20%

reduction in thickness and annealed at 1100°C for (a) 1 minute, (b) 5 minutes, (c) 10 minutes and (d) 30 minutes.

- Fig. 5: Comparison of 10% (a), 30% (b), 50% (c), and 70% (d) cold rolled samples annealed at 1100°C for 1 minute anneals of etched microstructure in (a)-(c) show no evidence of recrystallization. In (d), reveals some evidence of recrystallization noted by an increase in twin density and by a small decrease in grain size.
- Fig. 6: Microstructural comparison of 70% cold rolled/(1 minute) annealed samples heat treated at (a) 1100°C, (b) 1050°C, and (c) 1000°C. (a) grain size was approximately 40 μ m. (b) grain size equaled 25 μ m, (c) grain size equaled 19 μ m.
- Fig. 7: Illustration of original (a) and final (b) grain size. (a) average grain size is 40 μ m, and (b) average grain size is 15 μ m.
- Fig. 8: Annealing twin density versus grain size for variously thermomechanically processed 304 stainless steel samples (0.05% C).
- Fig. 9: Illustration of EPR-setup.
- Fig. 10: EPR scan produced by EPR test used to quantitatively calculate amount of precipitation or degree of sensitization (DOS) in austenitic stainless steels [18].
- Fig. 11: EPR-test scan for 15 μ m and 40 μ m (0 and 20% ϵ aged at 625°C) 304 stainless steel with 0.05% C (a). (b) Comparative optical metallographic views of EPR-test attack for 15 μ m (b), (c) and 40 μ m (d), (e). (b) No strain. (c) Strained 20%. (d) No strain. (e) Strained 20%.
- Fig. 12: TEM sample preparation sequence.
- Fig. 13: Examples of lamellar $M_{23}C_6$ carbide precipitation in 304 stainless steel. (a) Long lamellar precipitates along coherent twin boundary and away from the boundary for long, high-temperature aging. Note preponderance of dislocation loops on dislocations. (b) Lamellar carbides growing from non-coherent twin boundary in coherent twin boundary trace direction coincident with {111} plane trace (arrow). (c) Lamellar carbides growing in region adjacent to coherent twin boundary. Many precipitates do not appear to be associated with steps or interfaces, but grow

predominantly along a $\{111\}$ plane trace direction. The arrow marked "a" shows the precipitates in (a). (d) Lamellar $M_{23}C_6$ carbide growth out of steps in inclined coherent $\{111\}$ twin boundary (arrows). The growth direction is, however, coincident with another $\{111\}$ plane trace direction (marked with arrow at T).

Fig. 14: Lamellar $M_{23}C_6$ growth in relation to coherent annealing twin boundaries in (110) grain surface orientations. (a) Precipitate growing parallel to, and coincident with, the $(1\bar{1}1)$ twin plane trace at 90° to the (110) surface. (b) Precipitates growing from large non-coherent step and parallel to coherent annealing twin boundaries. (a) Strained 15% and aged at 625°C for 50 hours, and (b) aged 10 hours at 775°C . The growth direction is coincident with the trace of $(1\bar{1}1)$. The dotted arrow and upper arrow indicate the twin trace direction. (c) and (d) show lamellar $M_{23}C_6$ growing from inclined coherent twin boundaries in (110) orientation. The growth direction is coincident with the trace of (111) (arrows). Samples in (c) and (d) aged at 775°C for 10 hours.

Fig. 15: Lamellar growth of $M_{23}C_6$ from inclined (111) annealing twin boundary in (110) grain orientation showing alternate growth coincident with both $\{1\bar{1}1\}$ and $\{1\bar{1}\bar{1}\}$ planes at 90° to the (110) surface. These directions are denoted T90 and coincide with $\langle 112 \rangle$ directions shown dotted in the indexed diffraction net inserted. The corresponding (110) selected-area electron diffraction (SAD) pattern is also inserted in the image. Sample aged 10 hours at 775°C . Diffraction nets are after L.E. Murr, Electron and Ion Microscopy and Microanalysis, 2nd edition, Marcel Dekker Inc., New York, 1991, p. 698-704.

Fig. 16: $M_{23}C_6$ precipitate growth in relation to coherent $\{111\}$ annealing twin boundary in (112) grain surface orientation. (a) Grain segment shows precipitates growing parallel to 90° twin boundaries in T90 direction shown. (b) Grain segment shows precipitates growing out of inclined annealing twin boundary from non-coherent steps. The corresponding SAD pattern and indexed diffraction net are shown in inserts. Sample was aged 10 hours at 775°C .

Fig. 17: Intersection equilibrium of three general interfaces [20,21].

Fig. 18: Equilibrium twin-grain boundary intersection. The heavy vectors represent the associated non-zero torque components. Note: No

assumptions concerning the relationship of the true dihedral angles, Ω , were intended [20,21].

- Fig. 19: Equilibrium configuration at twin-grain boundary intersections [20].
- Fig. 20: Crystallographic misorientation at twin-grain boundary intersections. (a) Continuous misorientation of $\langle 110 \rangle$, $\Theta_{AB} = \Theta_{TAB}$; (b) discontinuous misorientation of $\langle 110 \rangle$, $\Theta_{AB} \neq \Theta_{TAB}$ [20,21].
- Fig. 21: Comparison of net effective torque distributions of geometrically and crystallographically specific twin/grain boundary intersections as illustrated in Fig. 19. The twins are in the (110) orientation [20].
- Fig. 22: Schematic of low and high torque twin/grain configurations for (110) orientation with corresponding diffraction net. (a) and (b) High torque configurations, with coherent twin plane inclined 90° to (110) orientation. (c) Low torque configuration with coherent twin boundaries inclined 35° to (110) orientation. Twin region is shaded.
- Fig. 23: Schematic of lamellar growth from or along high and low torque twin interfaces in (112) orientation. Also shown are the corresponding (112) diffraction nets. (a), (b), and (c) Low torque configuration with coherent twin boundary inclined (a), (b) 62° , and (c) 19° . (d) High torque twin configuration, with the coherent twin interface perpendicular to (112) surface orientation. (a)-(c) Where lamellar growth out of the inclined twin boundary along T90 direction would be expected. (d) Lamellar carbide growth parallel to coherent twin interface would be expected. Twin regions are shown shaded.
- Fig. 24: (100) grain surface orientation with $M_{23}C_6$ carbides nucleating and lying on the steps or ledges of an inclined coherent $\{111\}$ twin boundary (twin boundary inclined 54.7°) (a). The SAD pattern is shown inserted in (a) along with the corresponding indexed diffraction net. (b), (c), and (d) are blow ups of $M_{23}C_6$ precipitates sitting on the non-coherent steps of the twin boundary (top to bottom). Carbide growth coincident with a $\{111\}$ trace direction is not observed in the (100) orientation. Sample was aged 10 hours at 775°C .

LIST OF EQUATIONS

$$DOS = \frac{\frac{Q}{A}}{5.1 \times 10^{-4} e^{0.35G}} \quad (1)$$

$$\sum_{i=1}^3 [\gamma_i \sigma_i + (\sigma_i \times \mathbf{z}) \frac{\partial \gamma_i}{\partial \Omega_i}] = 0 \quad (2)$$

$$\begin{aligned} \gamma_{tb} + \gamma_{AB} \cos \Omega_1 + \gamma_{T_{AB}} \cos \Omega_2 + \sum M_I &= 0 \\ \gamma_{tb} + \gamma_{AB} \cos \Omega_4 + \gamma_{T_{AB}} \cos \Omega_3 + \sum M_{II} &= 0 \end{aligned} \quad (3)$$

$$\sum M_I = \frac{\partial \gamma_{AB}}{\partial \Omega} \sin \Omega_1 + \frac{\partial \gamma_{T_{AB}}}{\partial \Omega} \sin \Omega_2 \quad (4)$$

$$\sum M_{II} = \frac{\partial \gamma_{AB}}{\partial \Omega} \sin \Omega_4 + \frac{\partial \gamma_{T_{AB}}}{\partial \Omega} \sin \Omega_3 \quad (5)$$

$$\begin{aligned} \frac{\gamma_{tb}}{\gamma_{AB}} &= C_{AB} - \frac{1}{\gamma_{AB}} \left(\frac{\sum M_I \cos \Omega_3 - \sum M_{II} \cos \Omega_2}{\cos \Omega_3 - \cos \Omega_2} \right) \\ \frac{\gamma_{tb}}{\gamma_{T_{AB}}} &= C_{T_{AB}} - \frac{1}{\gamma_{T_{AB}}} \left(\frac{\sum M_I \cos \Omega_4 - \sum M_{II} \cos \Omega_1}{\cos \Omega_4 - \cos \Omega_1} \right) \end{aligned} \quad (6)$$

$$C_{AB} = \frac{\cos \Omega_2 \cos \Omega_4 - \cos \Omega_1 \cos \Omega_3}{\cos \Omega_3 - \cos \Omega_2} \quad (7)$$

$$C_{TAB} = \frac{\cos \Omega_2 \cos \Omega_4 - \cos \Omega_1 \cos \Omega_3}{\cos \Omega_1 - \cos \Omega_4} \quad (8)$$

$$\frac{\gamma_{tb}}{\gamma_{gb}} = \frac{1}{2} \sum_{i=1}^4 (-\cos \Omega_i) \quad (9)$$

$$\begin{aligned} \frac{\gamma_{tb} + \sum M}{\gamma_{AB}} &= C_{AB}, \\ \frac{\gamma_{tb} - \sum M}{\gamma_{TAB}} &= C_{TAB}, \end{aligned} \quad (10)$$

$$\sum M = \frac{\sum M_I \cos \Omega_3 - \sum M_{II} \cos \Omega_2}{\cos \Omega_3 - \cos \Omega_2} = - \frac{\sum M_I \cos \Omega_4 - \sum M_{II} \cos \Omega_1}{\cos \Omega_4 - \cos \Omega_1} \quad (11)$$

$$\frac{\gamma_{tb}}{\gamma_{gb}} = \frac{C_{AB} + C_{TAB}}{2} \quad (12)$$

$$\frac{\sum M}{\gamma_{gb}} = \left| \frac{C_{AB} - C_{TAB}}{2} \right| \quad (13)$$

CHAPTER ONE

INTRODUCTION

1.1 BACKGROUND NARRATIVE

Austenitic stainless steels (SS) are widely used for a variety of commercial applications *i.e.* piping and tubing components in nuclear reactors (especially hot water reactors) and refineries; and containers for storage and transport of nuclear and toxic waste. Thermomechanical processing, fabrication treatments, and handling along with operating conditions can produce strains and thermal conditions that initiate and accelerate microchemical and microstructural changes of the stainless steel components. In a corrosive environment, the microchemical and microstructural changes controlled by the grain boundaries present an occurring failure mechanism common in austenitic stainless steels known as stress corrosion cracking. An understanding of the vulnerability or susceptibility of the components to intergranular stress corrosion cracking is important for improvements and predictions of material reliability and performance during service.

Sensitization represents both a microstructural and a microchemical condition at an interface in stainless steels. Sensitization occurs due to the development of grain boundary or other interfacial chromium depletion (GBCD) zones. The depletion is induced by the precipitation of chromium-rich carbides on the grain boundaries or interfaces leaving the regions in and around the